Joint EUROGRAPHICS - IEEE TCVG Symposium on Visualization (2004)
O. Deussen, C. Hansen, D.A. Keim, D. Saupe (Editors)

Superquadric Tensor Glyphs

Gordon Kindlmann

School of Computing, University of Utah, United States

Abstract

Tensor field visualization is a challenging task due in part to the multi-variate nature of individual tensor samples. Glyphs convey tensor variables by mapping the tensor eigenvectors and eigenvalues to the orientation and shape of a geometric primitive, such as a cuboid or ellipsoid. Though widespread, cuboids and ellipsoids have problems of asymmetry and visual ambiguity. Cuboids can display misleading orientation for tensors with underlying rotational symmetry. Ellipsoids differing in shape can be confused, from certain viewpoints, because of similarities in profile and shading. This paper addresses the problems of asymmetry and ambiguity with a new tunable continuum of glyphs based on superquadric surfaces. Superquadric tensor glyphs enjoy the necessary symmetry properties of ellipsoids, while also imitating cuboids and cylinders to better convey shape and orientation, where appropriate. The new glyphs are demonstrated on fields of diffusion tensors from the human brain.

Categories and Subject Descriptors (according to ACM CCS): I.3.5 [Computer Graphics]: Curve, surface, solid, and object representations I.3.8 [Computer Graphics]: Applications

1. Introduction

Scientific visualization techniques convey structure and information over a range of scales, from large-scale patterns spanning an entire dataset, down to the individual samples comprising the dataset. When working with non-scalar data from medical imaging, such as diffusion or strain tensors from MRI [BMB94, AW01], low-level inspection of individual tensors is a necessary first step in exploring and understanding the data. Glyphs, or icons, depict multiple data values by mapping them onto the shape, size, orientation, and surface appearance of a base geometric primitive [PvWPS95]. Ideally, judicious composition of multiple glyphs from across the tensor field can hint at larger-scale features that may be subsequently explored and extracted with other visualization techniques, such as hyperstreamlines [DH95], stream-tubes, or stream-surfaces [ZDL03].

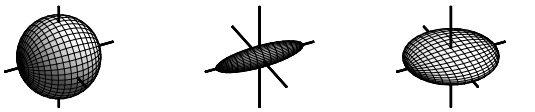

Isotropy (Spherical); Linear anisotropy; Planar anisotropy

Figure 1: *Three basic diffusion tensor shapes.*

Diffusion tensors can be represented as symmetric three-by-three matrices, which have three real, positive eigenvalues and three real-valued orthogonal eigenvectors [Str76]. A diffusion tensor $\mathbf{T}$ can be factored as $\mathbf{T} = \mathbf{R}\mathbf{\Lambda}\mathbf{R}^{-1}$ where $\mathbf{\Lambda}$ is a diagonal matrix of eigenvalues (by convention sorted $\lambda_1 \geq \lambda_2 \geq \lambda_3$), and $\mathbf{R}$ is a rotation matrix that transforms the standard basis onto the eigenvector basis. In this paper, "tensor shape" and "tensor orientation" refer to the eigenvalues and eigenvectors, respectively, of the tensor. The *anisotropy* of a tensor expresses the amount of variation in the eigenvalues. If tensors do not have any anisotropy ($\lambda_1 = \lambda_2 = \lambda_3$), they are considered spherical in shape. Anisotropic diffusion tensors can have linear shapes ($\lambda_1 > \lambda_2 = \lambda_3$), planar shapes ($\lambda_1 = \lambda_2 > \lambda_3$), or some combination; see Figure 1.

Glyph-based tensor visualization transforms an initial glyph geometry G into a tensor glyph $G_{\mathbf{T}}$ by

$$G_{\mathbf{T}} = \mathbf{R}\mathbf{\Lambda}G\,, \tag{1}$$

and then translating $G_{\mathbf{T}}$ to the field location of tensor $\mathbf{T}$ [SML03]. By *not* applying rotation $\mathbf{R}^{-1}$, the axis-aligned features of G (such as the edges of a unit cube) become representations in $G_{\mathbf{T}}$ of the tensor eigenvalues and eigenvectors. Different visualization effects are created by choosing different glyph geometries G, such as cubes [SML03], cylin-

ders [WLW00], or spheres [PB96, BP96, LAK*98]. Eigenvectors are known only up to line orientation (they have no signed direction), which constrains practical glyph geometries to shapes with 180 degree rotational symmetry. A computational advantage of using spheres (to create ellipsoidal glyphs) is that tensor diagonalization is not required, only matrix multiplication: $G_{\mathbf{T}} = \mathbf{R}^{-1}\mathbf{\Lambda}G = \mathbf{R}^{-1}\mathbf{\Lambda}\mathbf{R}G = \mathbf{T}G$.

The focus of this paper is the simple task of creating better tensor visualizations, with a new glyph geometry based on superquadric surfaces [Bar81]. Superquadric tensor glyphs build on previous research by Shaw et al. which applies superquadrics to glyph-based visualization [SEK*98, SHB*99, ERS*00, ES01]. They describe how parameterizing shape variations to encode data variables should enable effective and intuitive "perceptualizations", given that distinguishing shape from contours and shading is a *pre-attentive* process [PCC*92]. Offering a continuous two-parameter space of shapes, superquadrics are a natural choice for a tunable geometric primitive. The ability to discern differences between rendered superquadrics was experimentally quantified [SHB*99], and the superquadric glyphs were successfully used for document corpus visualization [SEK*98] and scientific visualization of magnetohydrodynamic flow [ERS*00, ES01].

The contribution of this paper is to use superquadrics as a *tensor* glyph rather than simply a multi-variate glyph. This requires selecting an intuitive subset of the superquadric parameter space to encode tensor shape, and ensuring that the display of tensor orientation faithfully conveys the symmetries that can arise in the tensor eigensystem.

2. Motivation

Evaluating existing tensor glyph geometries and their properties is facilitated with an intuitive domain that spans all possible tensor shapes. Such a domain is afforded by the geometric anisotropy metrics of Westin et al. [WPG*97]. Given the non-negative tensor eigenvalues $\lambda_1 \geq \lambda_2 \geq \lambda_3$, the metrics quantify the certainty (c) with which a tensor may be said to have a given shape:

$$c_l = \frac{\lambda_1 - \lambda_2}{\lambda_1 + \lambda_2 + \lambda_3}$$
$$c_p = \frac{2(\lambda_2 - \lambda_3)}{\lambda_1 + \lambda_2 + \lambda_3} \qquad (2)$$
$$c_s = \frac{3\lambda_3}{\lambda_1 + \lambda_2 + \lambda_3}$$

The three metrics add up to unity, and define a barycentric parameterization of a triangular domain, with the extremes of linear, planar, and spherical shapes at the three corners. The barycentric shape space has been used as the domain of transfer functions for direct volume rendering of diffusion tensors [KWH00], and as an intuitive basis of comparison between various anisotropy metrics [AHK*00]. The barycentric shape space is drawn in Figure 2 using cuboid glyphs to emphasize variations in aspect ratio over the triangular domain. Complete isotropy is at the top corner ($c_s = 1$), and anisotropy increases toward the lower edge.

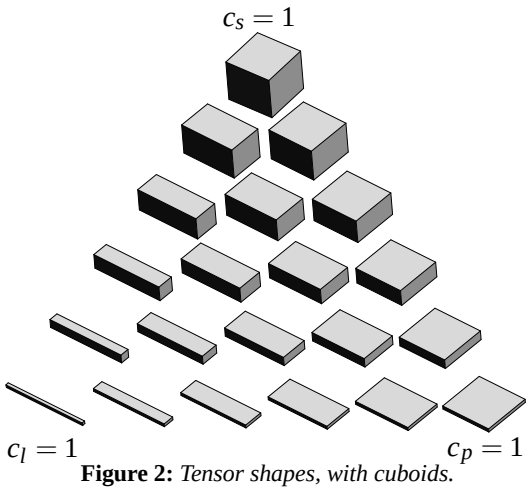

Figure 2: *Tensor shapes, with cuboids.*

Figure 2 illustrates a problem with cuboid glyphs: misleading depiction of under-constrained orientation. Because $c_p = 0 \Rightarrow \lambda_2 = \lambda_3$ for the linear shapes at the left edge of the triangle, computation of the corresponding eigenvectors $\mathbf{v}_2$ and $\mathbf{v}_3$ may return *any* two perpendicular vectors within the plane normal to the principal eigenvector $\mathbf{v}_1$. An analogous problem occurs with the planar shapes along the right edge of the triangle. The cuboid edges depict orientation with a visual clarity that is disproportionate to the low numerical accuracy with which the eigenvectors can be calculated [GL96]. For intermediate shapes, however, the sharp edges of the cuboids are good at depicting legitimate tensor orientation.

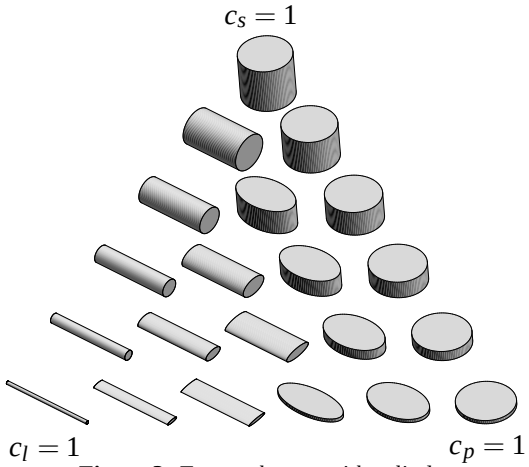

Figure 3: *Tensor shapes, with cylinders.*

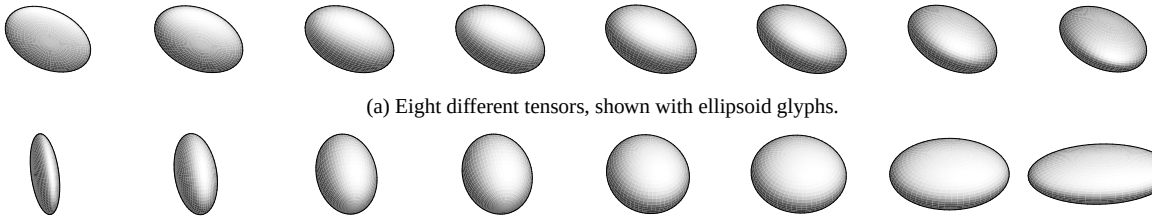

(a) Eight different tensors, shown with ellipsoid glyphs.

(b) Same eight glyphs, but with a different viewpoint.

Figure 5: *From some viewpoints, ellipsoids poorly convey tensor shape.*

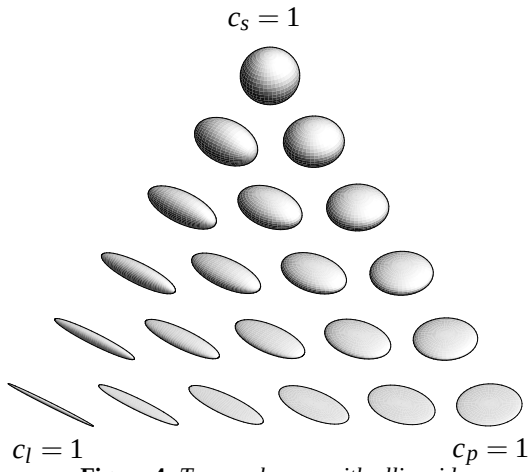

Figure 4: *Tensor shapes, with ellipsoids.*

Cylinder glyphs resolve this problem by aligning their axis of rotation along the eigenvector for which the numerical accuracy is greatest, as done in Figure 3. There is unfortunately a *discontinuity* problem, with a seam down the middle of the shape space. Arbitrarily small changes in the tensor shape can result in discontinuous changes in the glyph direction, even though the precise location of the seam is somewhat arbitrary. An alternate definition of c_l, c_p, c_s (normalized by λ_1 instead of $\lambda_1+\lambda_2+\lambda_3$ [WMK*99]) produces a slightly different distribution of intermediate shapes within an otherwise similar barycentric shape domain. In addition, because cylinders have only one axis of symmetry, cylindrical glyphs depict meaningless orientation for spherical tensors, which have no intrinsic orientation.

Ellipsoidal glyphs, shown in Figure 4, avoid all such symmetry problems. There is, however, a problem of visual ambiguity. Glyphs with differing *tensor* shapes exhibit similar *image-space* shapes, with only shading cues for disambiguation. Figure 5 demonstrates a pathological example. A wide range of tensors rendered with ellipsoid glyphs can appear similar from one viewpoint (Figure 5(a)), though they are clearly different when seen from another viewpoint (Figure 5(b)). This example is important because it demonstrates that even standard, intuitive glyph geometries can sometimes dramatically fail to properly convey data attributes.

3. Method

The problems of asymmetry and ambiguity can be addressed with a glyph geometry that changes according to the underlying tensor shape. Ideally, the best of Figures 2, 3, and 4 could be combined: cylinders for the linear and planar cases, spheres for the spherical case, and cuboids for intermediate cases, with smooth blending in between. The general strategy is that *edges on the glyph surface signify anisotropy*: anisotropy implies a difference in eigenvalues, which implies confidence in computing eigenvectors [GL96], which implies lack of rotational symmetry, which can be visually highlighted by a strong edge on the glyph surface. When two eigenvalues are equal, the indeterminacy of the eigenvectors is conveyed with a circular glyph cross-section.

Superquadrics accomplish this goal. They can be parameterized explicitly (for polygonal glyph representation):

$$\mathbf{q}_z(\theta,\phi) = \begin{pmatrix} \cos^\alpha\theta\sin^\beta\phi \\ \sin^\alpha\theta\sin^\beta\phi \\ \cos^\beta\phi \end{pmatrix}, \quad \begin{matrix} 0 \le \phi \le \pi \\ 0 \le \theta \le 2\pi \end{matrix}, \qquad (3)$$

where $x^\alpha = \mathrm{sgn}(x)|x|^\alpha$, or superquadrics may be represented implicitly (such as for raytracing):

$$q_z(x,y,z) = \left(x^{2/\alpha} + y^{2/\alpha}\right)^{\alpha/\beta} + z^{2/\beta} - 1 = 0. \qquad (4)$$

Figure 6 shows how α and β control superquadric shape. Superquadric tensor glyphs draw from a subset of these possibilities, defined by $\beta \le \alpha \le 1$. Note that the formulations of $\mathbf{q}_z$ and q_z are *not* symmetric with respect to axis permutation. Aside from the spherical case, the superquadrics may have continuous rotational symmetry around only the z axis (when $\alpha = 1$). Thus, as a counter-part, it is useful to define superquadrics around the x axis:

$$\mathbf{q}_x(\theta,\phi) = \begin{pmatrix} \cos^\beta\phi \\ -\sin^\alpha\theta\sin^\beta\phi \\ \cos^\alpha\theta\sin^\beta\phi \end{pmatrix}, \quad \begin{matrix} 0 \le \phi \le \pi \\ 0 \le \theta \le 2\pi \end{matrix}, \qquad (5)$$

$$q_x(x,y,z) = \left(y^{2/\alpha} + z^{2/\alpha}\right)^{\alpha/\beta} + x^{2/\beta} - 1 = 0. \qquad (6)$$

With these ingredients, superquadric tensor glyphs are

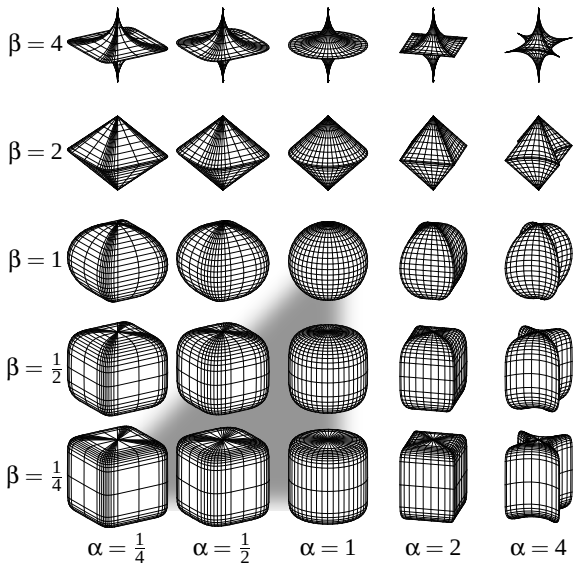

Figure 6: *Superquadrics defined by Equation 3. The gray triangle indicates the subset of the shape space employed by superquadric tensor glyphs. Edges indicate the tessellation resulting from uniform steps in ϕ and θ.*

now defined in terms of the geometric anisotropy metrics c_l, c_p, and a user-controlled edge sharpness parameter γ:

$$c_l \geq c_p \implies \begin{cases} \alpha = (1-c_p)^\gamma \\ \beta = (1-c_l)^\gamma \\ \mathbf{q}(\theta,\phi) = \mathbf{q}_x(\theta,\phi) \\ q(x,y,z) = q_x(x,y,z) \end{cases}$$

$$c_l < c_p \implies \begin{cases} \alpha = (1-c_l)^\gamma \\ \beta = (1-c_p)^\gamma \\ \mathbf{q}(\theta,\phi) = \mathbf{q}_z(\theta,\phi) \\ q(x,y,z) = q_x(x,y,z) \end{cases} \tag{7}$$

These equations define a base glyph geometry that is made into a tensor visualization via Equation 1. Figure 7 illustrates superquadric glyphs with the same tensors, lighting, and viewpoint as used in Figures 2, 3, and 4. The glyphs have the necessary symmetry properties of ellipsoids, but convey orientation and shape more clearly by imitating cylinders and cuboids where appropriate. The edge sharpness parameter γ controls how rapidly edges form as c_l and c_p increase, allowing the user to control the visual prominence of orientation information at low anisotropy levels. Ideally, application characteristics would enable an informed choice of γ: perhaps visualizations of noisy measurements would use a lower (more conservative) γ than visualizations of high-precision simulation data. Note that pure ellipsoids can be recovered as a special case, with $\gamma = 0$.

The rationale for how α and β are defined in Equation 7 can be understood with reference to Figure 6. For tensors that are more linear than planar ($c_l \geq c_p$), the glyph shape becomes more distinctly cylindrical as c_l increases and β decreases. True rotational symmetry is only present when $c_p = 0 \Rightarrow \alpha = 1$. As the planar component increases with c_p, the shape gradually tends away from rotational symmetry

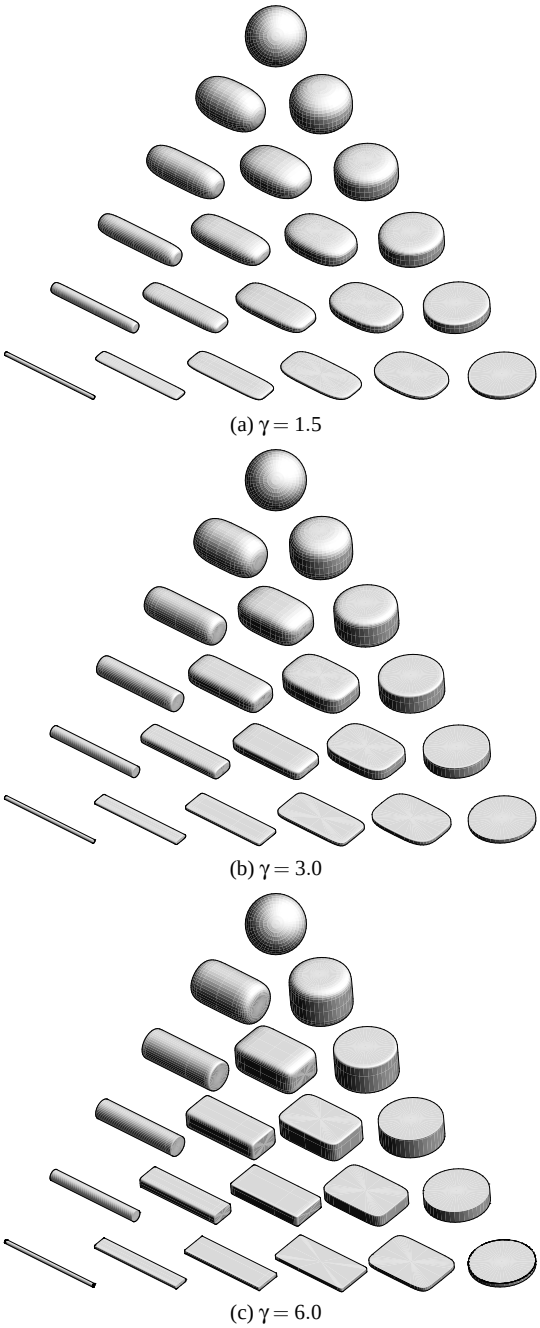

(a) $\gamma = 1.5$

(b) $\gamma = 3.0$

(c) $\gamma = 6.0$

Figure 7: *Tensor shapes, with superquadric glyphs, and three different values of edge sharpness parameter γ.*

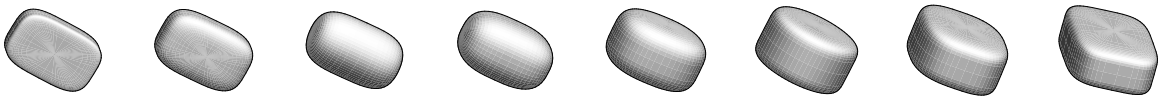

(a) Same tensors, viewpoint, and lighting as Figure 5(a), but with superquadric glyphs.

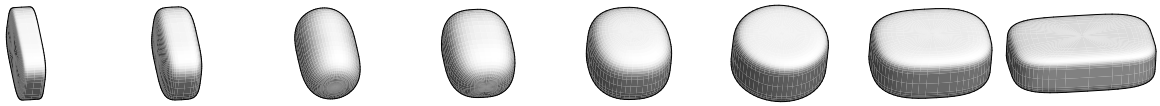

(b) Same as Figure 5(b), but with superquadric glyphs.

Figure 9: *Superquadrics convey shape differences more reliably than ellipsoids ($\gamma = 3$).*

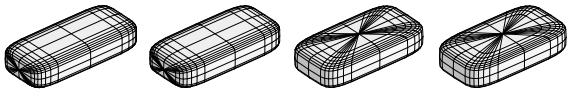

Figure 8: *Parameterization change across the linear/planar seam, from $c_l > c_p$ to $c_l < c_p$ ($\gamma = 3$).*

due to lower α, increasing the prominence of edges around the glyph circumference. Analogous reasoning holds for $c_l < c_p$. When $c_l = c_p$, $\alpha = \beta$, and $q_x(x,y,z) = q_z(x,y,z)$, in which case the x axis (Equations 5, 6) and the z axis (Equations 3, 4) superquadrics are identical. Thus, like cylinders (Figure 3), superquadric tensor glyphs *do* have a seam between the linear and planar sides of the shape space, but the seam is *mathematically* continuous. Figure 8 illustrates how the parameterization change may have an effect on a tessellation-based surface representation.

Figure 9 shows how superquadric glyphs are better at conveying shape than the ellipsoid glyphs in Figure 5, using the same tensors, viewpoint, and lighting. For example, the third and sixth glyphs from the left have precisely linear ($c_p = 0$) and planar ($c_l = 0$) shapes, respectively. The existence and the orientation of the resulting rotational symmetry is easier to see with superquadrics than with ellipsoids.

4. Results

Diffusion tensor magnetic resonance imaging (DT-MRI) of nerve tissue indirectly measures the fibrous structure of white matter by detecting the directionally constrained diffusion of water molecules within it [BMB94], resulting in a 3-D field of tensor values. Some DT-MRI voxels within the largest white matter structures (such as the corpus callosum) exhibit purely linear anisotropy, because the whole voxel region is homogeneously uni-directional. However, the complex branching and crossing of the white matter tracts, combined with the limited resolution of the DT-MRI modality, produces many measurements with significant planar anisotropy. Visualizing the locations and orientation of planar anisotropy is a step towards understanding the complex nature of white matter connectivity [WLW00].

For this task, Figure 10 compares the effectiveness of superquadric tensor glyphs and ellipsoids for visualizing a portion of an axial slice through a diffusion tensor dataset, centered on the right half of the splenium of the corpus callosum (the black region is the lateral ventricle). The background squares represent isotropy levels for each sample ("interesting" anisotropic tensors have a darker background and hence greater contrast with the glyph). Planarly anisotropic samples are located near the center of the image. With ellipsoids, it is difficult to discern which of the glyphs represent planar anisotropy, and it harder to appreciate the differences in shape that may occur between neighboring samples. Also, the straight edges of the linearly anisotropic superquadric glyphs provide a stronger orientation indication than possible with the rounded contours of ellipsoids.

In three-dimensional glyph-based visualizations of tensor volumes, it is important to restrict the number of glyphs, to avoid creating an illegible mass. In diffusion tensors, glyphs may be culled according to an anisotropy threshold (such as $c_l + c_p > 0.5$) so that isotropic tensors (belonging to gray matter or cerebral spinal fluid) are hidden, resulting in a coarse depiction of the major white matter pathways. Figure 11 uses this method to compare ellipsoid and superquadric glyphs for visualizing half of a diffusion tensor volume, centered again at the right half of the splenium of the corpus callosum. The superquadrics depict the amount and orientation of the planar component in the white matter more clearly than the ellipsoids. Comparing the planar orientation with the direction of adjacent linear anisotropy is an example of a visualization query which is better answered by the new glyph method.

5. Discussion

In comparing Figures 5(a) and 9(a), one could argue that various rendering effects would help clarify the shape differences among the ellipsoids: different lighting, specular highlights, or surface textures, for example. Interactive manipulation and stereo rendering would also help. On the other hand, these modifications would also benefit the de-

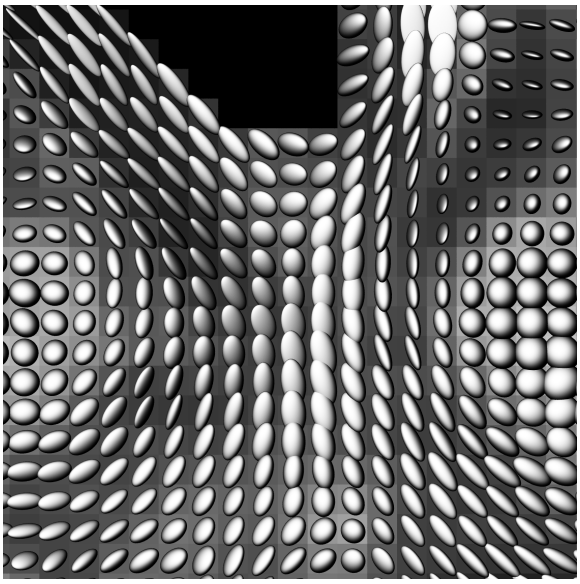

(a) Ellipsoids

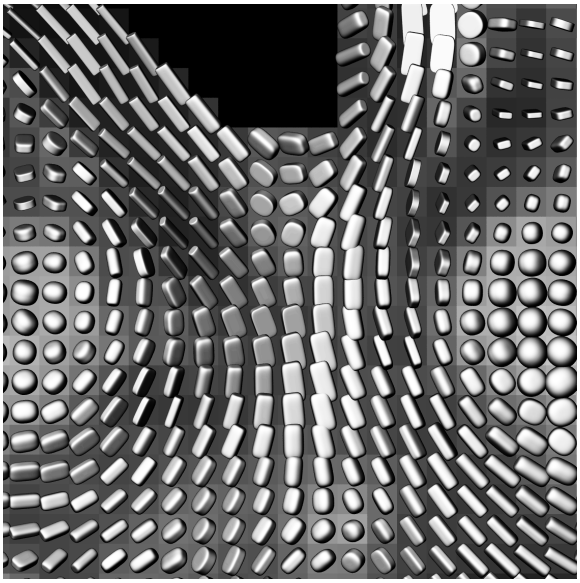

(b) Superquadrics ($\gamma = 3$)

Figure 10: *Slice of DT-MRI dataset of brain visualized with ellipsoids (top) and superquadrics (bottom).*

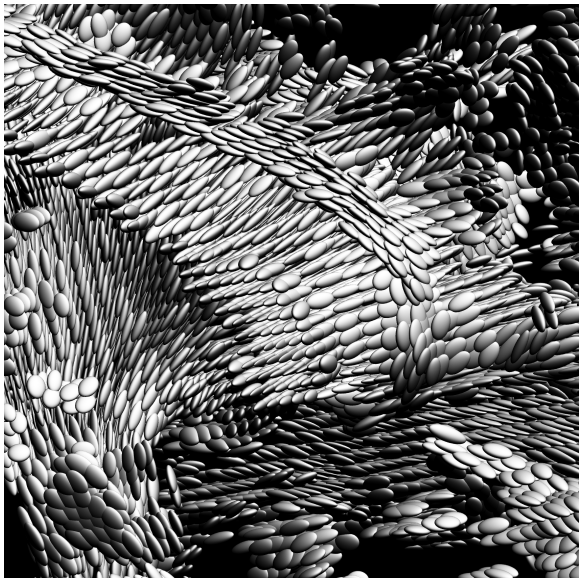

(a) Ellipsoids

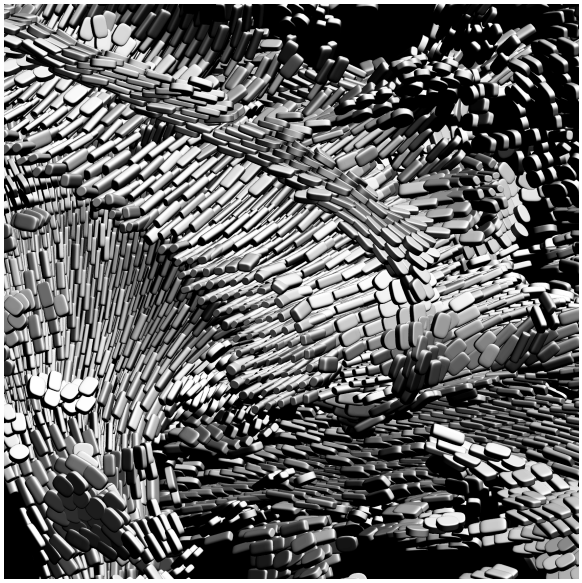

(b) Superquadrics ($\gamma = 3$)

Figure 11: *3-D region of DT-MRI dataset of brain visualized with ellipsoids (top) and superquadrics (bottom).*

piction of superquadrics. The same diffuse lighting and fixed viewpoint, which failed to distinguish the ellipsoid shapes, were sufficient to differentiate the superquadrics. Using data-driven variable geometry (Equation 7), *in addition* to the eigenvalue-based scaling, helps superquadric glyphs convey shape more explicitly than previous tensor glyphs. Fore-shortening of superquadric glyphs can still create visual ambiguity, although the range of affected viewpoints is smaller than with ellipsoids.

Starting with a more expressive glyph geometry allows further effects (color, textures, etc.) to be saved for encoding additional degrees of freedom that may be required in a more complex visualization application. The best way to enrich *three-dimensionsional* glyph-based visualizations with extra information is an important direction of future

work, since there are usually a number of related field values which should be visualized along with tensors. Inspiration may be drawn from artistic methods of painting and illustration [LAd*98, LKF*98, KML99, RLH*01]. Specifically, the composition of multiple glyphs into a depiction of larger-scale structure may benefit from context-sensitive and multi-scale variation of rendering style [HIK*01].

The incentive to create sharp edges in the superquadric glyphs was based on the observation that edges generate a strong visual cue for orientation. However, it is the mathematical property of rotational *symmetry* that constrains the glyph to be cylindrical and spherical according to the tensor eigensystem, and the idea of *continuity* that informed the design of an invisible seam through the middle of barycentric shape space. The combination of aesthetic judgment and mathematical constraint may be useful in the design of other visual abstractions for multi-variate and tensor visualization.

Acknowledgements

Funding was provided by the University of Utah Research Foundation PID 2107127 and the National Institutes of Health/NCRR, 5 P20 HL68566-03 and 5 P41 RR12553-05. Brain dataset courtesy of Andrew Alexander at the W. M. Keck Laboratory for Functional Brain Imaging and Behavior, University of Wisconsin-Madison

Every figure in this paper can be regenerated exactly with open-source software and public datasets; see <http://www.sci.utah.edu/~gk/vissym04>.

References

[AHK*00] ALEXANDER A., HASAN K., KINDLMANN G., PARKER D., TSURUDA J.: A geometric comparison of diffusion anisotropy measures. *Magnetic Resonance in Medicine* (2000), 283–291. 2

[AW01] ALETRAS A., WEN H.: Mixed echo train acquisition displacement encoding with stimulated echoes: an optimized dense method for in vivo functional imaging of the human heart. *Magnetic Resonance in Medicine 46*, 3 (2001), 523–534. 1

[Bar81] BARR A.: Superquadrics and angle-preserving transformations. *IEEE Computer Graphics and Applications 18*, 1 (1981), 11–23. 2

[BMB94] BASSER P., MATTIELLO J., BIHAN D. L.: Estimation of the effective self-diffusion tensor from the NMR spin-echo. *Journal of Magnetic Resonance B 103*, 3 (1994), 247–254. 1, 5

[BP96] BASSER P., PIERPAOLI C.: Microstructural and physiological features of tissues elucidated by quantitative-diffusion-tensor MRI. *Journal Magnetic Resonance B 111*, 3 (1996), 209–219. 2

[DH95] DELMARCELLE T., HESSELINK L.: A unified framework for flow visualization. In *Computer visualization: graphics techniques for scientific and engineering analysis*, Gallagher R. S., (Ed.). CRC Press, 1995, pp. 129–170. 1

[ERS*00] EBERT D., ROHRER R., SHAW C., PANDA P., KUKLA J., ROBERTS D.: Procedural shape generation for multi-dimensional data visualization. *Computers and Graphics 24* (2000), 375–384. 2

[ES01] EBERT D., SHAW C.: Minimally immersive flow visualization. *IEEE Transactions on Visualization and Computer Graphics 7*, 4 (2001), 343–350. 2

[GL96] GOLUB G., LOAN C. V.: *Matrix Computations*. Johns Hopkins University Press, Baltimore and London, 1996, ch. 7. 2, 3

[HIK*01] HEALEY C., INTERRANTE V., KREMERS D., LAIDLAW D., RHEINGANS P.: Nonphotorealistic rendering in scientific visualization. In *Course Notes of SIGGRAPH 2001, Course 32* (2001). 7

[KML99] KIRBY M., MARMANIS H., LAIDLAW D.: Visualizing multivalued data from 2D incompressible flows using concepts from painting. In *Proceedings of IEEE Visualization 1999* (1999), pp. 333–340. 7

[KWH00] KINDLMANN G., WEINSTEIN D., HART D. A.: Strategies for direct volume rendering of diffusion tensor fields. *IEEE Transactions on Visualization and Computer Graphics 6*, 2 (April-June 2000), 124–138. 2

[LAd*98] LAIDLAW D., AHRENS E., DAVIDKREMERS, AVALOS M., READHEAD C., JACOBS R.: Visualizing diffusion tensor images of the mouse spinal cord. In *Proceedings of IEEE Visualization 1998* (October 1998), pp. 127–134. 7

[LAK*98] LAIDLAW D., AHRENS E. T., KREMERS D., ANDR.E. JACOBS M. A., READHEAD C.: Visualizing diffusion tensor images of the mouse spinal cord. In *Proceedings IEEE Visualization 98* (1998), pp. 127–134. 2

[LKF*98] LAIDLAW D., KREMERS D., FRANKEL F., INTERRANTE V., BANCHOFF T.: Art and visualization: Oil and water? In *Proceedings IEEE Visualization 98* (1998), pp. 507–509. 7

[PB96] PIERPAOLI C., BASSER P.: Toward a quantitative assessment of diffusion anisotropy. *Magnetic Resonance in Medicine* (1996), 893–906. 2

[PCC*92] PARKER A., CHRISTOU C., CUMMING B., JOHNSTON E., HAWKEN M., ZISSERMAN A.: The analysis of 3D shape: Psychological principles and neural mechanisms. In *Understanding Vision*, Humphreys G., (Ed.). Blackwell, Oxford, 1992, ch. 8. 2

[PvWPS95] POST F., VAN WALSUM T., POST F., SILVER D.: Iconic techniques for feature visualization. In *Proceedings IEEE Visualization 95* (1995), pp. 288–295. 1

[RLH*01] RHYNE T., LAIDLAW D., HEALEY C., INTERRANTE V., DUKE D.: Realism, expressionism, and abstraction. In *Proceedings IEEE Visualization 01* (2001), pp. 523–526. 7

[SEK*98] SHAW C., EBERT D., KUKLA J., ZWA A., SOBOROFF I., ROBERTS D.: Data visualization using automatic, perceptually-motivated shapes. In *Proceedings of Visual Data Exploration and Analysis* (1998), SPIE. 2

[SHB*99] SHAW C., HALL J., BLAHUT C., EBERT D., ROBERTS D.: Using shape to visualize multivariate data. In *Proceedings of the 1999 Workshop on New Paradigms in Information Visualization and Manipulation* (1999), ACM Press, pp. 17–20. 2

[SML03] SCHROEDER W., MARTIN K., LORENSEN B.: *The Visualization Toolkit: An Object Oriented Approach to Graphics*. Kitware, Inc., Clifton Park, New York, 2003, ch. 6. 1

[Str76] STRANG G.: *Linear Algebra and Its Applications*. Academic Press, Inc., Orlando, Florida, 1976, ch. 5.5. 1

[WLW00] WIEGELL M., LARSSON H., WEDEEN V.: Fiber crossing in human brain depicted with diffusion tensor MR imaging. *Radiology 217* (2000), 897–903. 2, 5

[WMK*99] WESTIN C.-F., MAIER S., KHIDHIR B., EVERETT P., JOLESZ F., KIKINIS R.: Image processing for diffusion tensor magnetic resonance imaging. In *Medical Image Computing and Computer-Assisted Intervention (MICCAI)* (1999), pp. 441–452. 3

[WPG*97] WESTIN C.-F., PELED S., GUBJARTSSON H., KIKINIS R., JOLESZ F.: Geometrical diffusion measures for MRI from tensor basis analysis. In *Proceedings 5th Annual ISMRM* (1997). 2

[ZDL03] ZHANG S., DEMIRALP C., LAIDLAW D. H.: Visualizing diffusion tensor MR images using streamtubes and streamsurfaces. *IEEE Transactions on Visualization and Computer Graphics 9*, 4 (October 2003), 454–462. 1